Earthquake early warning using future generation gravity strainmeters

K. Juhel[1,2,3], J. P. Ampuero[4], M. Barsuglia[2], E. Chassande-Mottin[2], D. Fiorucci[2], J. Harms[5,6], J.-P. Montagner[1], M. Vallée[1], and B. F. Whiting[7]

[1]Institut de Physique du Globe de Paris, Paris, France
[2]AstroParticule et Cosmologie, Paris, France
[3]Université Sorbonne Paris Cité, Paris, France
[4]Université Côte d'Azur, IRD, CNRS, Observatoire de la Côte d'Azur, Géoazur, Sophia Antipolis, France
[5]Gran Sasso Science Institute, L'Aquila, Italy
[6]INFN, Laboratori Nazionali del Gran Sasso, Assergi, Italy
[7]Department of Physics, University of Florida, Gainesville, Florida, USA

Key Points:

- Future high-precision gravity strainmeters could record prompt gravity signals before the seismic waves arrival during an earthquake rupture
- Planned sensitivity is sufficient to observe gravity perturbations from earthquakes of magnitude larger than 7 at distances up to 1000 km
- Gravity-based warning system could perform faster detection and magnitude estimation of large earthquakes compared to conventional systems

Corresponding author: Kévin Juhel, juhel@ipgp.fr

Abstract

Recent studies reported the observation of prompt elastogravity signals during the 2011 M9.1 Tohoku earthquake, recorded with broadband seismometers and gravimeter between the rupture onset and the arrival of the seismic waves. Here we show that to extend the range of magnitudes over which the gravity perturbations can be observed and reduce the time needed for their detection, high-precision gravity strainmeters under development could be used, such as torsion bars, superconducting gradiometers or strainmeters based on atom interferometers. These instruments measure the differential gravitational acceleration between two seismically isolated test masses, and are designed to observe signals around 0.1 Hz. We show that these instruments should be able to detect prompt gravity perturbations induced by earthquakes larger than M7, up to 1000 km from the earthquake centroid within P-waves travel time and up to 120 km within the first 10 seconds of rupture onset, provided a sensitivity in gravity strain of 10^{-15} $\mathrm{Hz}^{-1/2}$ at 0.1 Hz can be achieved. The analysis involves simulations of the expected gravity strain signals based on an analytical model of gravity perturbations generated by fault rupture in a homogeneous half-space. As an immediate application, we discuss the possibility to improve current earthquake-early warning systems (EEWS). Our results suggest that, in comparison to conventional P-wave-based EEWS, a gravity-based warning system could perform faster detections of large off-shore subduction earthquakes (at least larger than M7.4). Gravity strainmeters could also perform earlier magnitude estimates, within the duration of the fault rupture, and therefore complement current tsunami warning systems.

1 Introduction

During an earthquake rupture, fault slip and the propagation of seismic waves redistribute masses within the Earth. The mass redistribution generates a dynamic long-range perturbation of the Earth's gravity, which propagates at speed-of-light and is thus recordable before the arrival of the direct seismic waves (Harms et al., 2015; Montagner et al., 2016; Vallée et al., 2017). These prompt gravity perturbations have been observed with broadband seismometers and superconducting gravimeter during the M9.1 Tohoku-oki earthquake (Montagner et al., 2016; Vallée et al., 2017). The potential contribution of such signals to tsunami early warning is substantial: such observations would indeed

have provided an early estimate of a magnitude greater than M9 within three minutes of the earthquake origin time.

However, two factors hinder the observation of prompt elastogravity signals with ground-based seismometers: the background seismic noise and a partial cancellation between the gravitational perturbation and its induced ground acceleration, whose difference is recorded by the instruments (Heaton, 2017; Vallée et al., 2017). Elastogravity signal detection based on individual seismometer records is thus limited to earthquakes with magnitudes larger than 8.

One approach to improve earthquake monitoring capabilities is to overcome the limitations associated with the use of ground-coupled seismometers and gravimeters, by measuring the differential gravitational acceleration between two seismically isolated test masses. This detector concept is known as a gravity strainmeter. Gravity strainmeters designed to observe signals at 0.1 Hz, within the frequency range needed to detect earthquake-related gravity changes, are being developed to observe gravitational waves (GW) sources in the sub-Hz domain (Harms et al., 2013) and are briefly reviewed in Section 2. We note that the sub-Hz instruments are much smaller, lighter than the instruments developed for high-frequency (> 100 Hz) GW detection (1-m scale compared to 1-km scale). Moreover, GW detection has very stringent requirements, thus the sensitivity needed for earthquake detection should be achieved at an earlier stage of the instrument development. In contrast to seismometers, gravity strainmeters implement sophisticated seismic isolation schemes to measure differential displacements or rotations between test masses. The differential measurement rejects partially the background seismic noise and the gravity-induced inertial acceleration, which are similar for the two masses. Thus, for measuring earthquake-induced gravity perturbations, gravity strainmeters may be considered as a natural step toward improved sensitivities.

In this article we evaluate quantitatively the improvement of earthquake early warning systems (EEWS) that could be obtained, in principle, by using the gravity strainmeters under development. Current EEWS are automatic systems formed by seismometers and communication networks, intended to detect the occurrence of an earthquake before the arrival of ground-shaking waves and to disseminate the information to the population (R. M. Allen, Gasparini, Kamigaichi, & Bose, 2009; Heaton, 1985). Conventional EEWS rely on detecting the seismic P-waves, which travel at several km/s and are roughly

twice as fast as the usually stronger, more damaging S-waves. Since changes in gravity propagate at the speed of light, a gravity-based warning system could give a potential gain in the warning times, with respect to conventional EEWS. An expected consequence is a reduction of the blind zone of an EEWS, i.e. the area around the epicenter of an earthquake that cannot receive a warning before the arrival of the S-phase. We show that a gravity-based warning system could perform faster detections of large off-shore subduction earthquakes and early magnitude estimates, available as soon as the rupture stops.

2 High-precision gravity strainmeters

2.1 Detector concepts

Gravity strainmeters are instruments designed to measure gravity strain $\boldsymbol{h}$, which is the second time-integral of the spatial-gradient of gravity acceleration $\delta\boldsymbol{g}$:

$$\boldsymbol{h}(\boldsymbol{r},\, t) = \int_0^t \int_0^{\tau'} \boldsymbol{\nabla}\delta\boldsymbol{g}(\boldsymbol{r},\, \tau)\; d\tau d\tau' \,. \tag{1}$$

Very sensitive gravity strainmeters have been developed in the context of GW detection. In their advanced configurations, laser-interferometric GW detectors LIGO (Abbott et al., 2009) and Virgo (Accadia et al., 2011) have designed strain sensitivities of 10^{-23} $\mathrm{Hz}^{-1/2}$ between about 30 Hz and 2000 Hz. Due to their poor sensitivity in the sub-Hz region, advanced GW detectors cannot be used to measure gravity perturbations from earthquakes. In fact, in order to produce noticeable terrestrial gravity noises in the sensitive frequency band of advanced detectors, it has been shown that typical density perturbations have to be generated very close to the suspended test masses, i.e. within a few tens of meters (Driggers, Harms, & Adhikari, 2012; Harms, DeSalvo, Dorsher, & Mandic, 2009). This means that terrestrial gravity perturbations that will be measured in advanced detectors are likely to be of little interest in geophysics.

To access the sub-Hz region, which is very rich in GW sources, three concepts for 0.1 Hz gravity gradiometers are currently under development: superconducting gradiometers (SGG) (Moody, Paik, & Canavan, 2002; Paik et al., 2016), torsion-bar antennas (e.g. TOBA (Ando et al., 2010) or TorPeDO (McManus et al., 2017)) and atom-interferometric gradiometers (Geiger, 2017; Hohensee et al., 2011). In the following, we will refer to these detectors as GG10, i.e. gravity gradiometers with high-sensitivity for signals with periods around 10 seconds.

All three concepts present novel solutions to the mitigation of seismic noise, which would otherwise exceed gravity signals by many orders of magnitude. The superconducting gradiometer achieves seismic-noise reduction by common-mode rejection in the differential readout of test-mass positions relative to a common, stiff reference frame. Torsion-bar antennas can be engineered with very low torsion resonance frequency, which constitutes an efficient passive filter of rotational seismic displacement. The rejection of translational displacement noise is obtained by reading-out the differential signal from two suspended bars (or a bar with respect to a suspended platform) (Shimoda, Aritomi, Shoda, Michimura, & Ando, 2018). Atom-interferometric gradiometers read out the displacement between freely falling ultracold atom clouds, which also provides partial immunity to seismic noise. In order to reduce the requirements of the seismic rejection, additional passive or active seismic-isolation techniques can be used (Winterflood, 2001).

The most sensitive instrument so far is the superconducting gradiometer with a strain sensitivity of about 10^{-10} $\mathrm{Hz}^{-1/2}$ at 0.1 Hz (Moody et al., 2002). However, extensive gain in experience with these technologies has led to defining more ambitious strain-sensitivity targets: 10^{-15} $\mathrm{Hz}^{-1/2}$ at 0.1 Hz (Ando et al., 2010; Hogan et al., 2011; Hohensee et al., 2011). It will be shown in section 3.2 that such design sensitivities are sufficient for the detection of prompt gravity perturbations from earthquakes (of magnitude $>$ M6.5). It should be noted that all three concepts are also being considered as candidates for future, sub-Hz GW detectors with more ambitious sensitivity targets (10^{-20} $\mathrm{Hz}^{-1/2}$ at 0.1 Hz) (Harms et al., 2013; Paik et al., 2016).

2.2 Detector sensitivity models

The response of different types of gravity strainmeters to gravity-gradient fluctuations is not identical (Harms, 2015). The consequence is that instrumental noise spectra differ qualitatively between detector types. Current experimental efforts for all prototypes have the common gravity-strain sensitivity target of about 10^{-15} $\mathrm{Hz}^{-1/2}$ at 0.1 Hz. Below 0.1 Hz, instrumental noise in all concepts rises steeply. The high-frequency noise spectra differ more strongly. While it is expected that instrumental noise of the superconducting gradiometer keeps falling above 0.1 Hz (in units of gravity strain) (Moody et al., 2002), torsion-bar antennas have a flat noise spectrum above 0.1 Hz (Shoda et al., 2014), and atom-interferometric gradiometers reach their best sensitivity only within small frequency bands (Cheinet et al., 2008).

For the purpose of this paper, we will use simplified sensitivity models to represent all GG10 concepts. The simplified approach chosen here is to assume that the sensitivity is proportional to $1/f^2$ at low frequencies, that signal contributions below 0.01 Hz are not considered (GG10 detectors are not designed for such low-frequency observations), and that instrumental noise at high frequencies is frequency-independent. To estimate the detection horizon of gravity strainmeters to earthquakes, four sensitivity models are tested: flat strain sensitivity of 10^{-15} $Hz^{-1/2}$ above 0.05 and 0.1 Hz (models 1 and 2, respectively), 10^{-14} $Hz^{-1/2}$ above 0.05 Hz (model 3) and 5×10^{-17} $Hz^{-1/2}$ above 0.5 Hz (model 4). The resulting sensitivity curves are shown in Fig. 1, along with TOBA Phase III and SGG sensitivity curves. For the SGG sensitivity curve, a 20 kg mass and a 2 meters-long baseline are used, along with an energy resolution E_A of the superconducting quantum-interference device (SQUID) 10 times better than current commercial DC SQUID values (Griggs, Moody, Norton, Paik, & Venkateswara, 2017).

2.3 Local gravity noise

GG10 detectors have different limiting noise sources and experimental challenges to reach the target of 10^{-15} $Hz^{-1/2}$ at 0.1 Hz, specific to each detector. A detailed description of the contributions of various noise sources to the target sensitivity and the techniques to reduce them can be found in the references for each detector. But a gravity noise foreground is common to all the detectors: the local gravity noise (LGN). The LGN has several contributions: seismic LGN produced by density changes in the ground due to seismic waves; atmospheric LGN generated by density fluctuations in the atmosphere due to, for instance, infrasounds, temperature changes and turbulences; LGN associated with human activity (Harms, 2015). This noise couples with the detector in a way completely equivalent to the earthquake signal: it is then impossible to shield the detector from it.

Provided that the detector is located at a sufficiently remote site to avoid transient contributions to gravity as could be produced by cars or trucks passing close to the detector, the LGN contributions that need to be mitigated further are of seismic and atmospheric origin. One way to mitigate the LGN is to select seismically and atmospherically quiet sites. To some extent, this can be achieved by constructing the detector underground, but since seismic and sound waves have long wavelengths around 0.1 Hz, the

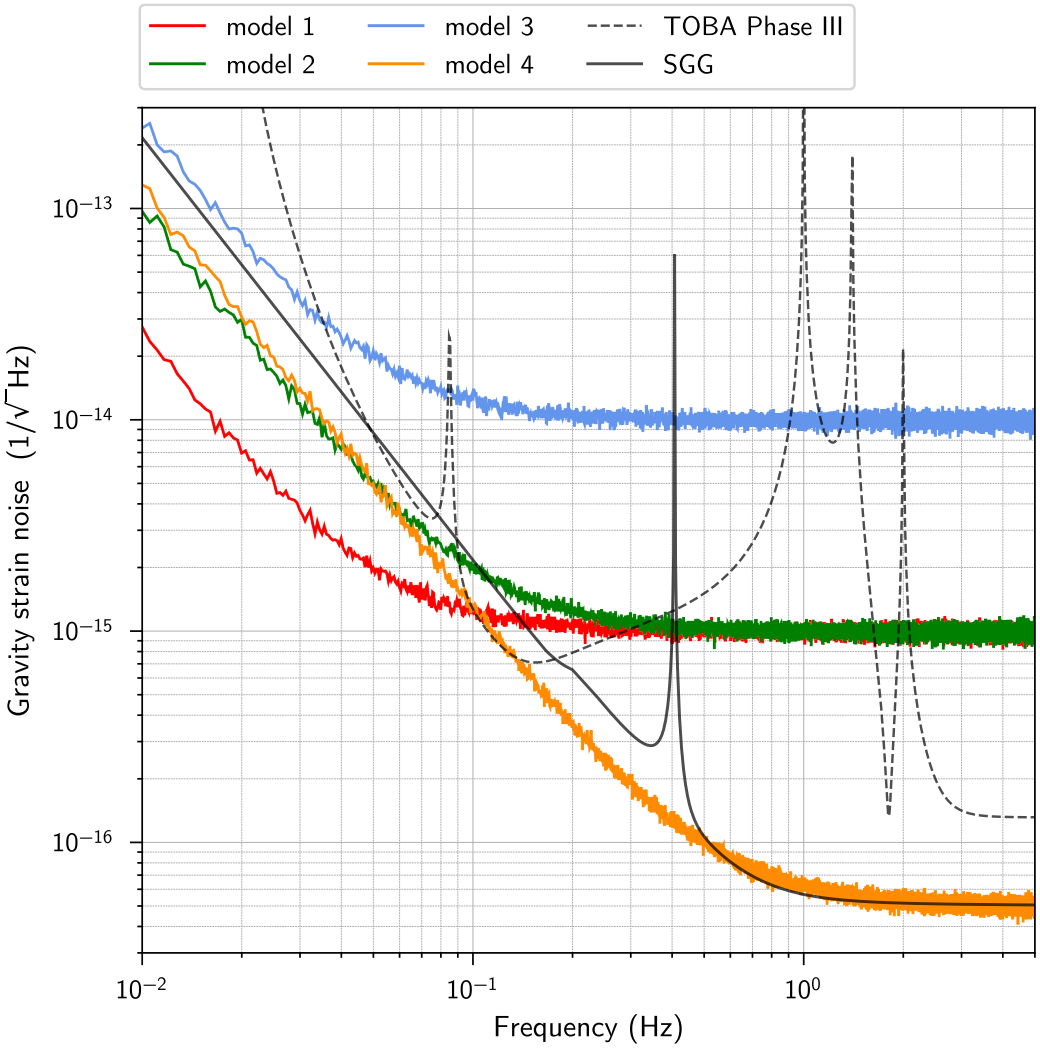

Figure 1. Simplified sensitivity models for gravity gradiometers designed for high-sensitivity around 10 seconds (GG10), along with TOBA Phase III and SGG sensitivity curves. Several noisefloors (10^{-14}, 10^{-15} and 5×10^{-17} $\mathrm{Hz}^{-1/2}$) and corner frequencies (0.05, 0.1 and 0.5 Hz) are considered to estimate the detection horizon of future GG10 detectors to earthquake ruptures.

associated gravity disturbances are only weakly suppressed underground for feasible detector depths (Beker et al., 2011; Fiorucci, Harms, Barsuglia, Fiori, & Paoletti, 2018).

As an alternative solution to LGN mitigation, it was proposed to coherently subtract LGN using data from arrays of environmental sensors, such as seismometers for the seismic LGN and microphones for the infrasound atmospheric LGN (Cella, 2000; Harms & Paik, 2015). The idea is to obtain sufficient information about local mass-density fluctuations to calculate an accurate estimate of the associated LGN. This method exploits correlations between environmental sensors and the GG10 detector by calculating a Wiener filter whose output corresponds to the optimal (linear) estimate of the LGN (Driggers et al., 2012).

Based on models for the infrasound atmospheric LGN from Fiorucci et al. (2018) and the even smaller seismic LGN (see for instance Fig. 9 from Harms et al. (2013)), we note that above a few mHz these LGN components should not affect significantly the GG10 sensitivity required for the earthquake-related signal detection. This will be shown in Section 3.2. Nevertheless, we point out that the use of average seismic and infrasound spectra to estimate the LGN components can lead to underestimate the challenge associated with this noise. With this in mind, while work is ongoing to reduce further these noise contributions, it is assumed for the remainder of the paper that all forms of LGN lie below the instrumental noise at all frequencies.

3 Detectability of prompt gravity strain perturbations

3.1 Optimal matched-filter detection and signal-to-noise ratio

In order to assess the detectability of the gravity perturbation, we compute the signal-to-noise ratio (SNR) obtained with each gravity strainmeter described in section 2.2. To compute the SNR, we consider detection via optimal matched-filtering (Jaranowski & Królak, 2012), which is based on the cross-correlation between the gravity data and a template of the expected gravity strain perturbation. Template-matching techniques have been widely used in modern seismology to detect earthquakes with low SNRs (Frank et al., 2014; Gibbons & Ringdal, 2006; Shelly, Beroza, & Ide, 2007), and in astrophysics to detect coalescing compact binaries (Bose, Dayanga, Ghosh, & Talukder, 2011; Pai, Dhurandhar, & Bose, 2001).

For simplicity, the detector noise is here assumed to be Gaussian and stationary. Before the matched-filter is applied, both the template and the detector data are passed through a whitening filter, in order to obtain an approximately frequency-independent detector noise spectral density. The whitening filter is a highpass filter (Butterworth, 2 poles) whose corner frequency is the corner frequency of the considered instrument sensitivity model. Once the noise spectrum is uniformly distributed, the optimum filter is the time-reversed, whitened template. The SNR is then defined as the ratio between the output of the optimal matched-filter in the presence of a signal and the standard deviation of the output in the absence of a signal.

3.2 SNR at P-wave arrival time and 10 seconds after onset time

In order to compute the gravity signal templates for a class of earthquakes, a model for source time functions (STF) should be used. In this section we adopt a self-similar source model, which implies that the initial phase of a large-magnitude event is identical to that of a lower-magnitude event. While this universal rupture-initiation behavior is still debated (Colombelli, Zollo, Festa, & Picozzi, 2014; Meier, Ampuero, & Heaton, 2017; Meier, Heaton, & Clinton, 2016), such hypothesis is a classic assumption and represents the worst-case scenario for EEW. Here, the following self-similar model of seismic moment rate function $\dot{\mathrm{M}}_0$ is employed:

$$\dot{\mathrm{M}}_0(t) = a\,\frac{\mathrm{M}_0}{\mathrm{T}}\,(t/\mathrm{T})^2 \tag{2}$$

if $0 < t < \mathrm{T}$, and

$$\dot{\mathrm{M}}_0(t) = a\,\frac{\mathrm{M}_0}{\mathrm{T}}\,\left(1-(t/\mathrm{T}-1)^2\right)^6 \tag{3}$$

if $\mathrm{T} < t < 2\mathrm{T}$, where T is the half-duration of the rupture and a a scalar. We adopt the empirical magnitude-duration relation $2\mathrm{T} = (\mathrm{M}_0 \,/\, 10^{16}\,\mathrm{N.m})^{1/3}$ (Houston, 2001). The shape of the first half of this source time function is that of a circular crack with constant rupture speed and uniform stress drop. The second half is a polynomial approximation to the stopping stage in the moment rate function of the circular crack model of Madariaga (1976).

Based on this source model, we compute gravity strain perturbations for various magnitude-distance pairs, induced by a dip-slip event with angles (strike, dip, rake) = (180°, 10°, 90°). We consider magnitudes ranging from 5 to 9.1, and epicentral distances ranging from 75 to 1100 km. Ten different azimuths are considered, ranging from 270

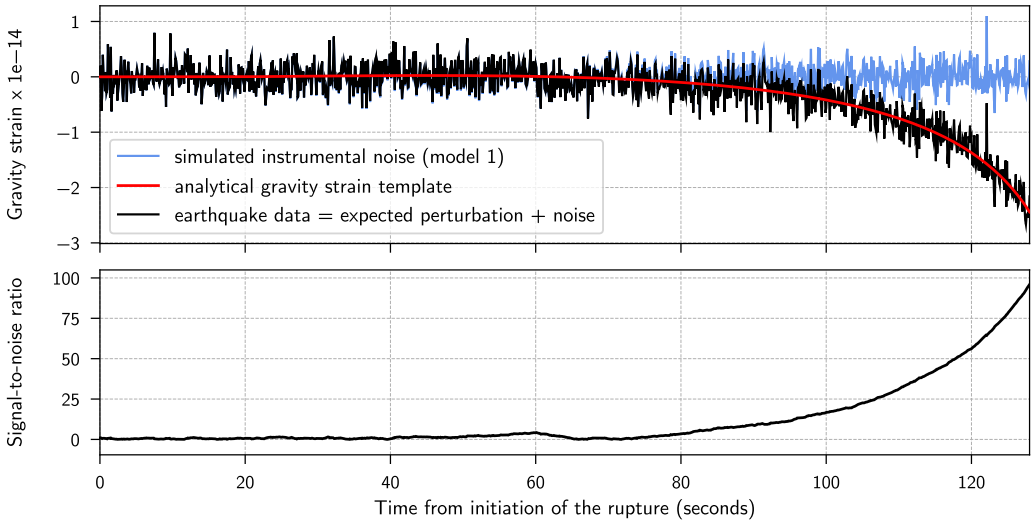

Figure 2. Earthquake data and SNR time series during a M7.5 earthquake. (top) Whitened gravity strain data (black curve, XZ component) recorded by a model-1 gravity strainmeter located 1000 km away from the epicenter of a M8 dip-slip earthquake. The recorded data is obtained as the sum of the whitened instrumental noise (blue curve) and the whitened gravity strain perturbation (red curve, Harms, 2016). (bottom) Corresponding signal-to-noise ratio, defined as the ratio between the data filtered with the time-reversed template, and the standard deviation of the noise filtered with the time-reversed template.. The time series are truncated at P-wave arrival time, 128 seconds after the earthquake onset time.

to 360° such that half of the down-dip part of the radiation pattern is computed (the remaining half being infered by symmetry).

We first compute vertical (Z) gravity perturbations δg_z in a half-space model, using the analytical formulations developed by Harms (2016). The medium is defined by a P-wave velocity of 7.8 km/s and an S-wave velocity of 4.4 km/s, such that the P-wave arrival times for stations located 250 to 1100 kilometers away from the epicenter are globally comparable to travel times obtained in a more realistic Earth model, such as PREM (Dziewonski & Anderson, 1981). The XZ and YZ components of the gravity gradient tensor $\boldsymbol{\nabla}\delta g_z$ are then obtained by the finite difference of gravity perturbations computed at two close locations, aligned along the East-West (X-) and North-South (Y-) directions. Two integrations over time then lead to the associated gravity strain perturbations.

We add simulated instrumental noises, for the four different sensitivity models considered in section 2.2. For each magnitude and distance, we then apply the optimal matched-filter (i.e the whitened template used to compute the synthetic earthquake data) with a finite duration time-window and normalize by the standard deviation of the matched-filter output in the absence of signal. The result is a set of continuous time series of SNRs, with values fluctuating around 1 during the absence of a signal. An example of (XZ) gravity strain data and corresponding SNR time series are shown in Fig. 2, for a model-1 gravity strainmeter located 1000 km away from the epicenter of a magnitude M7.5 earthquake, in the along-dip direction. At P-wave arrival time, 128 seconds after the earthquake onset time, the SNR reaches ~ 100.

For each epicentral distance and magnitude, the SNRs accumulated within the travel time of P-waves to the detector are shown in Fig. 3. Each point of the contour plot is the average SNR obtained for ten different azimuths, two components of the gravity strain tensor (XZ and YZ) and a hundred different realizations of the detector noise. As expected, SNRs globally increase with increasing magnitudes. Two lobes of high SNRs are observed at high magnitudes, separated by a region of lower SNR where the gravity strain records reach a zero-crossing at P-wave arrival time. The zero-crossing is observed at longer epicentral distances for higher magnitudes, since higher magnitudes are associated to STF with longer half-duration (which acts as a low-pass filter on the gravity strain record). High SNRs (> 50) are reached within P-wave travel times for detector models with high-sensitivity around 0.1 Hz (models 1, 2 and 4). The highest ratios (>100) are measured with the instrument 1, which displays the highest sensitivity at low frequencies. For this model, SNR larger than 10 are reached for every earthquake of magnitude larger than 7, up to 1000 kilometers from the epicenter. An improved high-frequency sensitivity (from model 2 to model 4) leads to slightly higher SNRs for epicentral distances below 300 km.

The SNRs of signals measured within the first 10 seconds of a fault rupture are shown in Fig. 4. The SNRs increase with decreasing epicentral distances, and saturate for event magnitudes greater than 6.5 as a consequence of self-similarity (the moment rate functions of earthquakes of larger magnitudes are identical in the initial 10 seconds). Accordingly, earthquake detection with SNR higher than 10 based on only 10 seconds of data would require next-stage detectors to be about 100 km or closer to the hypocenter, independent of the event magnitude above M6.5 (models 1 and 4). Improved low-frequency

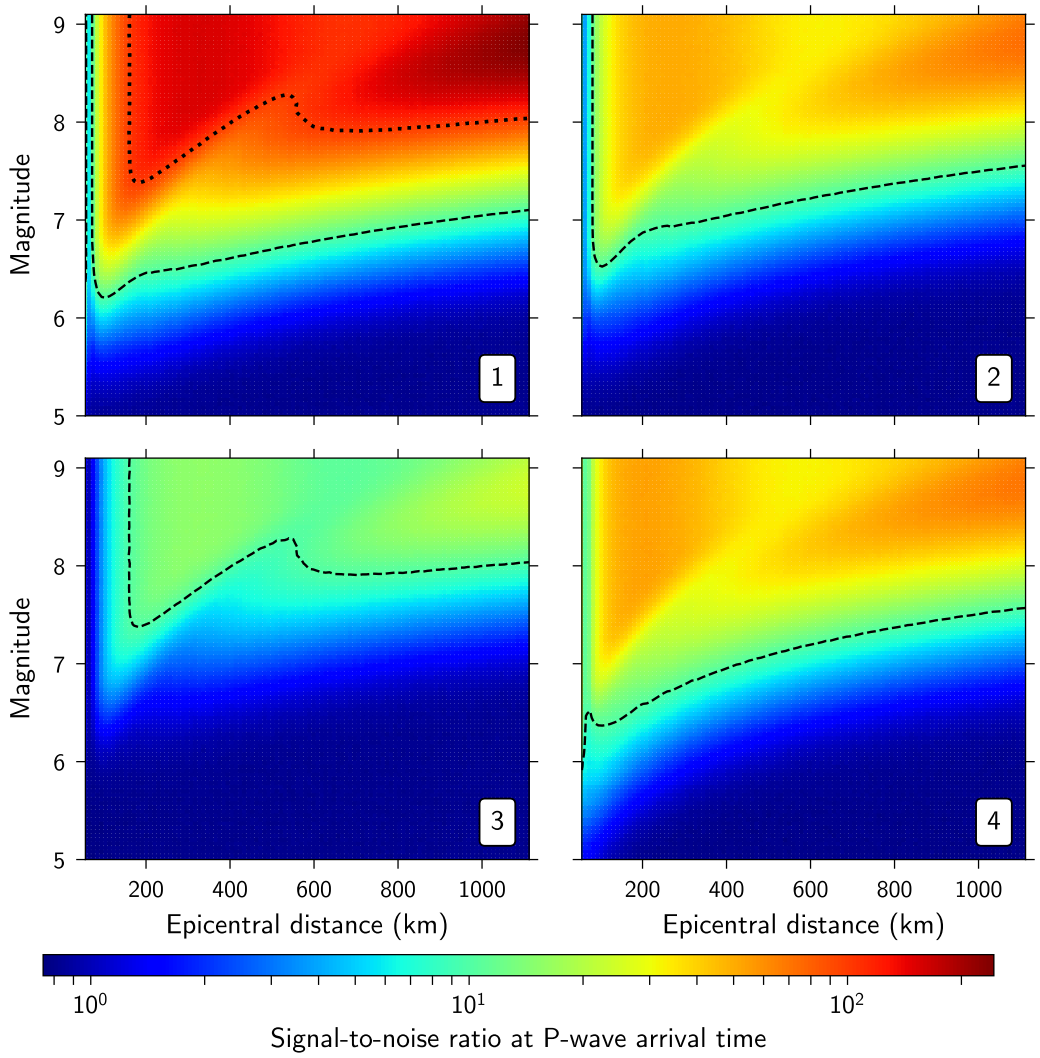

Figure 3. Signal-to-noise ratio accumulated within P-wave travel time to the detector as a function of event magnitude and distance of the detector. The sensitivity models 1 to 4 of the next-stage gravity strainmeter are used (see section 2.2). Contour lines are for SNR = 10 (dashed) and 100 (dotted).

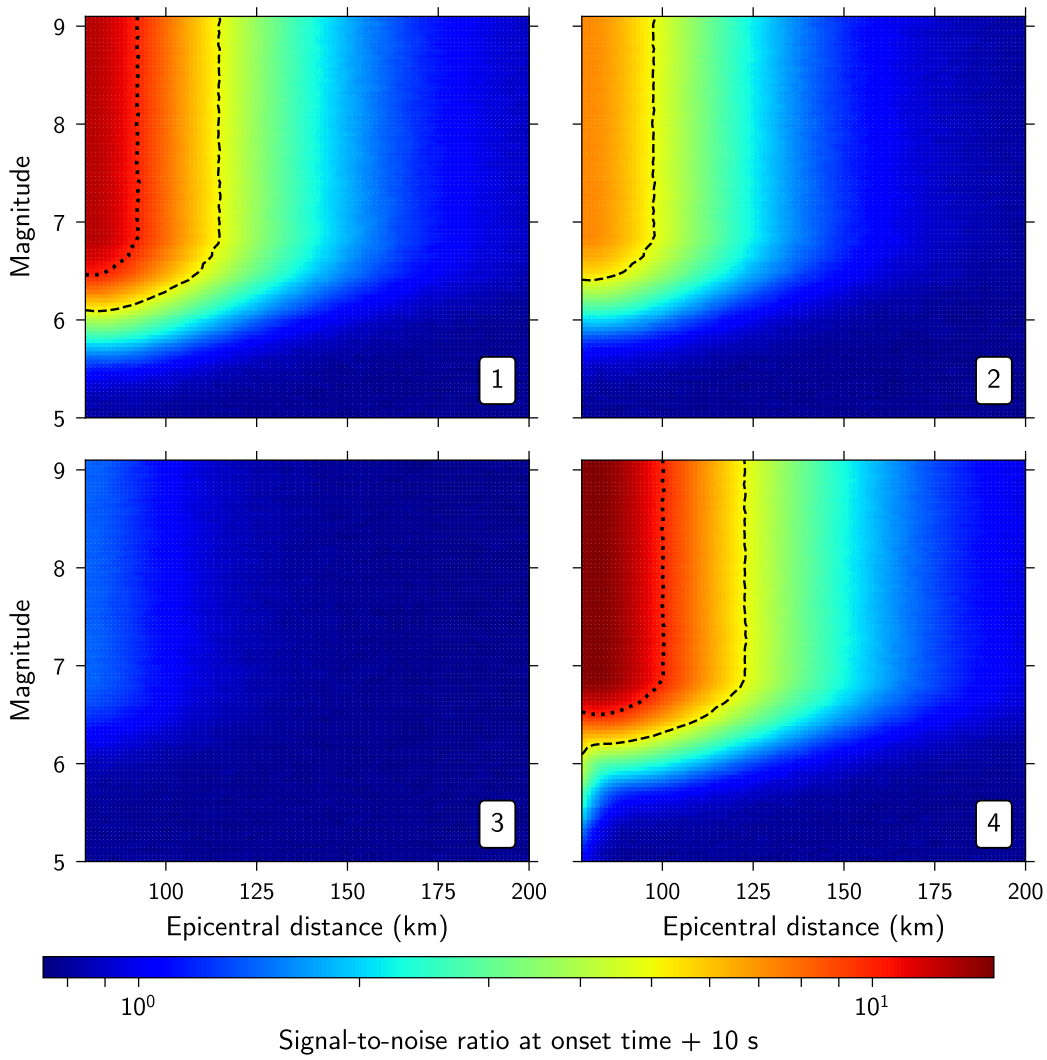

Figure 4. Signal-to-noise ratio accumulated within the first 10 seconds after onset time, as a function of event magnitude and distance of the detector. The sensitivity models 1 to 4 of the next-stage gravity strainmeter are used (see section 2.2). Contour lines are for SNR = 5 (dashed) and 10 (dotted).

sensitivity (from model 2 to model 1) and high-frequency sensitivity (from model 2 to model 4) lead to improved SNRs.

While the detector corresponding to sensitivity model 3 (10^{-14} $\mathrm{Hz}^{-1/2}$ above 0.1 Hz) should detect events of magnitude M7.5 and above with SNR higher than 10 at P-wave arrival time (see Fig. 3), its use for EEW purposes appears to be limited (see Fig. 4). Prompt detections of earthquake-induced perturbations thus require the strain sensitivity target of 10^{-15} $\mathrm{Hz}^{-1/2}$ at 0.1 Hz.

The magnitudes of the first seconds of real earthquakes can significantly exceed the predictions of our self-similar source model (the 10-seconds SNRs saturate at magnitude 6.5). Thus, our source model can be considered as conservative for the estimation of SNR.

4 Potential application to earthquake early warning

The foregoing analysis shows that large earthquakes can induce significant gravity strain perturbations at long distances. These perturbations are essentially instantaneous, compared to seismic wave propagation time-scales. This property opens new prospects for the rapid estimate of earthquake source parameters and its application to the mitigation of earthquake and tsunami hazards. Here we discuss how this feature can be exploited to improve the capabilities of one of the most challenging applications in real-time seismology: earthquake early warning. In particular, we demonstrate the potential contribution to EEW of a regional network of gravity strainmeters.

4.1 Earthquake early warning systems

EEWS aim to detect the occurrence of an earthquake as soon as possible and broadcast an alert before the arrival of strong seismic shaking (R. M. Allen et al., 2009; Böse et al., 2014). They are a crucial tool to reduce damage and injuries from earthquakes. Existing EEWS are based on the difference of propagation speed between P-waves (fast, compressional) and S-waves (slower, shear) and on the fact that the strongest, most damaging ground motions are carried by S-waves and (even slower) surface waves.

On-site EEWS exploit the first few seconds of recorded ground motions (mainly P-wave) to estimate the expected ground shaking at the recording site (Kanamori, 2005; Zollo, Amoroso, Lancieri, Wu, & Kanamori, 2010). Estimates of the event location or magnitude are not necessarily made, such that no regional warnings are issued. Network-

based EEWS use multiple stations closest to the epicenter to estimate the event location, final magnitude and origin time before issuing a regional warning. Recent advances include algorithms and systems to account for the finite rupture size of large-magnitude events (e.g. Böse, Heaton, & Hauksson, 2012; Meng, Allen, & Ampuero, 2014; Minson, Murray, Langbein, & Gomberg, 2014).

The finite speed of seismic waves, the density of a seismic network, signal transmission delays, the minimal number of stations and signal duration required to estimate earthquake magnitude impose together a minimum on the warning time and on the distance that can be reached by an early warning. This minimum distance is the distance travelled by the S-waves at the time the warning is issued and defines the "blind zone" of an EEWS. Seismic travel times can be longer than 10 seconds for offshore or deep earthquakes: if an EEWS could be based on other geophysical signals with negligible travel time, valuable seconds could be gained. The instantaneous character of earthquake-induced gravity perturbations in principle offers an opportunity for such a gain.

Every saved second can have an important impact in terms of life preservation and earthquake mitigation, since advanced warning enables the launching of automatic prevention systems and the implementation of safety procedures (R. Allen, 2013). Short though it may seem, a warning time of a few seconds is longer than the response time of automated control systems that mitigate the impact of strong shaking on industrial facilities and infrastructure, such as Japanese bullet trains (Nakamura & Saita, 2007) or on gas and chemical supply systems and high-precision equipment in a Japanese semiconductor factory (Takamatsu, 2009). A few seconds gain in warning time can also enable or enhance significantly personal protective actions (e.g. most people can perform "Duck, Cover and Hold On" within 10 seconds after warning) (Porter, 2016). Moreover, the radius of the blind zone would be reduced. Considering that earthquake intensity is much higher at closer distance, this could result in a significant potential reduction of damage and life loss.

4.2 Real-time event detection with a gravity-based EEWS

4.2.1 Template matched-filtering and event detection

A gravity-based EEWS must first detect in real-time the initiation of an earthquake, based on a few seconds of continuous recordings by a regional network of gravity strain-

meters. We propose to assess the real-time likelihood of an earthquake rupture with a network-based matched-filter approach. Our template matched-filter relies on the computation of an average likelihood ratio (LR), basically a multi-channel SNR, among all pairs of sensors and components, computed in a running window as:

$$\mathrm{LR}(t) = \frac{\sum_i^{N_i} \sum_j^{N_j} \sum_n^{N} \mathrm{h}_{ij}(n\Delta t)\, \hat{\mathrm{s}}_{ij}(t - n\Delta t)}{\sqrt{\sum_i^{N_i} \sum_j^{N_j} \sum_n^{N} \mathrm{h}_{ij}(n\Delta t)^2}} \,. \tag{4}$$

h and ŝ are respectively the pre-whitened gravity strain template and pre-whitened, normalized continuous gravity strain record. ŝ is normalized such that its root mean square is unity in the absence of signal. i and j are indices for the sensors and components, N_i and N_j their corresponding numbers, while N stands for the number of samples in the sliding window. We note that, in contrast to what is classicaly used in seismology, there is no moveout in equation (4) to describe the differential arrival times on each station, since the earthquake-induced gravity perturbations propagate almost instantaneously to each gravity strain sensor.

Detection is based on a threshold applied to the LR values, and can be achieved by communicating data in real-time to a central processor or by implementing a more distributed communication scheme. The threshold is set by the end-user, depending on his tolerance level on false alarm rates and missed event rates.

4.2.2 Template database and event parameter estimation

A regional EEWS requires not only earthquake detection, but also an estimate of the source location, origin time, fault mechanism and seismic moment. This requires a library of signal templates, which is here composed of a collection of analytical gravity strain Green's functions, computed between the sensor locations and a source location grid. The gravity strain Green's functions are later convolved with a catalog of moment rate source time functions. We drop here the self-similar source model, as we are interested in the detection of every event, including those that do not respect self-similarity. Thus, a whole range of source half-durations is considered for a given template final moment (set to 1 N.m). Two types of onset are considered, with moment rate STF growing either linearly (isosceles triangular STF) or quadratically with time (STF described in equations (2) and (3)).

Source parameters and their uncertainties are then estimated in real-time as the parameters corresponding to the template with the highest LR, and could be provided to the EEWS decision module with regular updates every second or so. The use of a pre-computed template database reduces computational times for real-time operation.

An estimate of the earthquake magnitude can be obtained from the scaling factor α between the optimal template $\mathbf{t}$ (whose seismic moment is prescribed by the user) and the actual recorded gravity strain $\mathbf{s}$. The factor α is the least-squares estimate of the scaling factor between $\mathbf{t}$ and $\mathbf{s}$, averaged over the sensors and components:

$$\alpha(t) = \frac{1}{N_i}\frac{1}{N_j}\sum_{i}^{N_i}\sum_{j}^{N_j}\frac{\sum_n^N \mathrm{t}_{ij}(n\Delta t)\,\mathrm{s}_{ij}(t-n\Delta t)}{\sum_n^N \mathrm{t}_{ij}(n\Delta t)^2}\,. \tag{5}$$

The estimated earthquake moment is α times the template moment.

Templates are correlated fully or by parts, such that we monitor the growth of the rupture as soon as it begins. We point out that in comparison to conventional EEW systems which estimate the final magnitude of an earthquake, our proposed system estimates the instantaneous magnitude, i.e. the seismic moment released up to the time the estimate is made. In principle, at stations that are located beyond the P-wave front at the earthquake end-time, rupture arrest can be diagnosed, and the final magnitude estimated.

4.2.3 Rupture scenario

To demonstrate the potential of a gravity-based EEWS, we focus on large off-shore subduction earthquakes. We thus consider in this subsection rupture scenarii of the 2011 M9.1 Tohoku-oki earthquake and its M7.3 foreshock, as it would have been recorded by networks of gravity strain sensors. Two different networks of three gravity strainmeters are considered, one close to the ruptured areas ($\sim$ 250 km from the epicenter), the other at regional distances ($\sim$ 1100 km from the epicenter).

Gravity strain data is obtained through the sum of the analytical perturbations and the simulated instrumental noises for two components of the gravity strain tensor, as already performed in section 3. We choose here to consider the intermediate detector sensitivity model 1, with a gravity-strain sensitivity of 10^{-15} Hz$^{-1/2}$ at 0.1 Hz.

We use the Global Centroid Moment Tensor (GCMT, Ekström, Nettles, & Dziewoński, 2012) parameters for the epicenter coordinates ((37.52°N, 143.05°E) for the Tohoku event, (38.56°N, 142.78°E) for its foreshock) and fault geometries ((strike/dip/rake) = (203°/10°/88°)

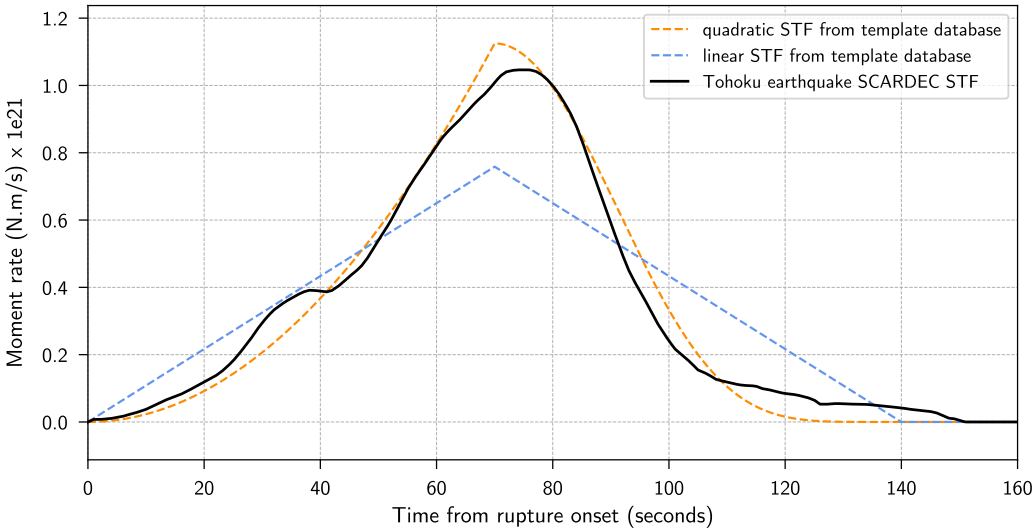

Figure 5. SCARDEC solution for the moment-rate STF of the M9.1 Tohoku earthquake (solid line), along with the closest templates (dashed lines). STF templates grow either linearly (blue line) or quadratically (orange line) with time. STFs are normalized to 1 N.m in the template database, but are here scaled to the event final moment for plotting purposes.

for the Tohoku event, (189°/12°/78°) for its foreshock), and the source time functions from the SCARDEC catalog (Vallée, Charléty, Ferreira, Delouis, & Vergoz, 2011).

In order to build a template database, gravity strain Green's functions are computed analytically for three different dip-slip fault mechanisms, which approximate the subduction context near the Japan Trench (strike = 180°, 190° or 200°, dip = 10° and rake = 90°, depth 20 km). Two types of STF onset (linear and quadratic) and source half-durations ranging from 2 to 90 seconds are considered. It should be noted that the actual source solutions for the Tohuku event and its foreshock are not in the present template database. Examples from the STF database, along with SCARDEC solution for the Tohoku earthquake are plotted in Fig. 5. Additional priors based on the geometry of major active faults in the area, and a catalog of moment rate functions from past earthquakes could complement the template database in the future.

As an example, the gravity strain recordings 15 seconds after the Tohoku earthquake onset time, along with the corresponding optimal template are shown for one rupture scenario in Fig. 6. The earthquake would have been detected with a high LR (> 50) and accurate estimates for the epicenter location, onset time and released magnitude,

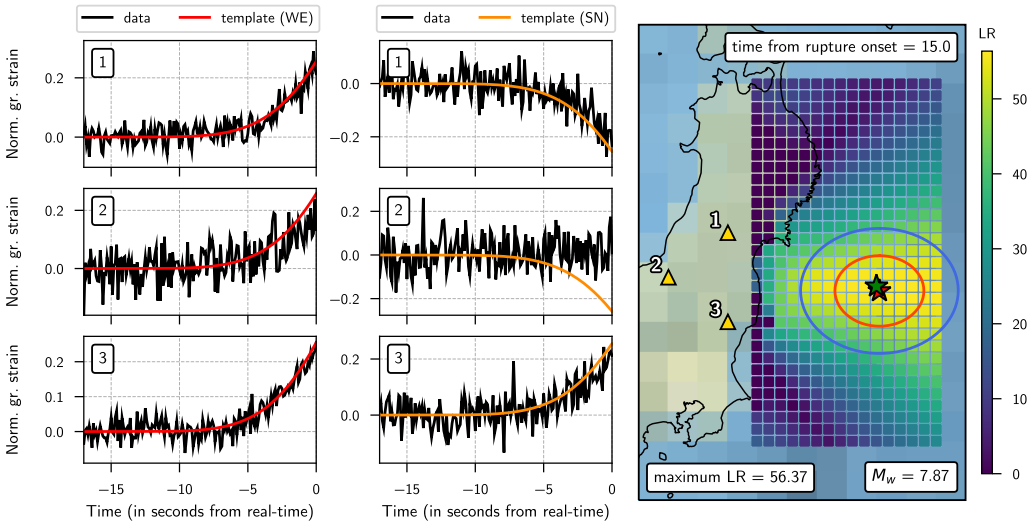

Figure 6. Offline real-time detection, source location and magnitude estimation of the M9.1 Tohoku earthquake, 15 seconds after onset time. (left) Gravity strain recording (black lines), along with the best-fitting gravity strain template (red and orange lines). Both gravity strain record and template are normalized by their respective root mean square, for plotting purposes. (right) The red and green stars represent the earthquake epicenter location and its estimated location, respectively. 15 seconds after onset time, P- (blue) and S-wavefronts (red) have not yet reached the coasts, while a M7.9 earthquake is detected with a high likelihood ratio (> 50), close to the actual M7.7 magnitude.

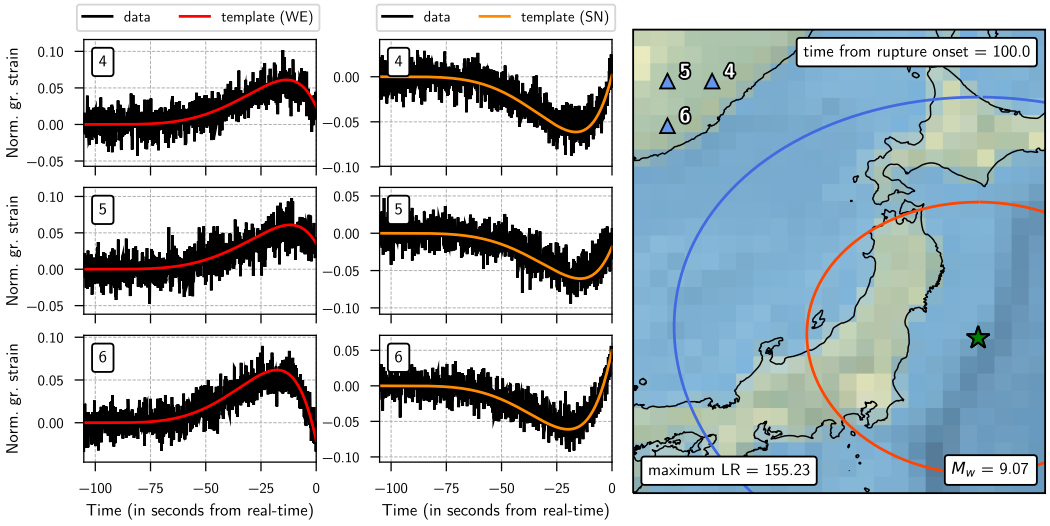

Figure 7. Offline real-time magnitude estimation of the M9.1 Tohoku earthquake, 100 seconds after onset time. (left) Gravity strain recording (black lines), along with the best-fitting gravity strain template (red and orange lines). Both gravity strain record and template are normalized by their respective root mean square, for plotting purposes. (right) The epicenter location is supposed to be known. 100 seconds after onset time, a > M9 earthquake is detected.

five seconds before the P-waves even hit the Japanese coastlines. The optimal template corresponds to a rupture still ongoing, while the lower bound magnitude estimate of the rupture (> M8.7) is high enough to issue a regional warning.

The seismic P-wavefront reaches sensors considered in Fig. 6 before the Tohoku earthquake end-time, such that an estimate of the earthquake final magnitude cannot be made based on these sensors. A network of gravity strainmeters located further away from the rupture area (beyond $\sim$ 1000 km) could monitor the whole rupture. This is the case for the second network we considered. See for instance the gravity strain recordings and corresponding optimal templates 100 seconds after onset time in Fig. 7.

A hundred different rupture scenarii for the M9.1 Tohoku earthquake and its M7.3 foreshock have been simulated, with a different random realization of instrument noise computed for each scenario. The earthquake magnitudes are estimated in real-time by the two networks, the corresponding results are displayed in Fig. 8. The input seismic moment functions from the SCARDEC database are accurately retrieved.

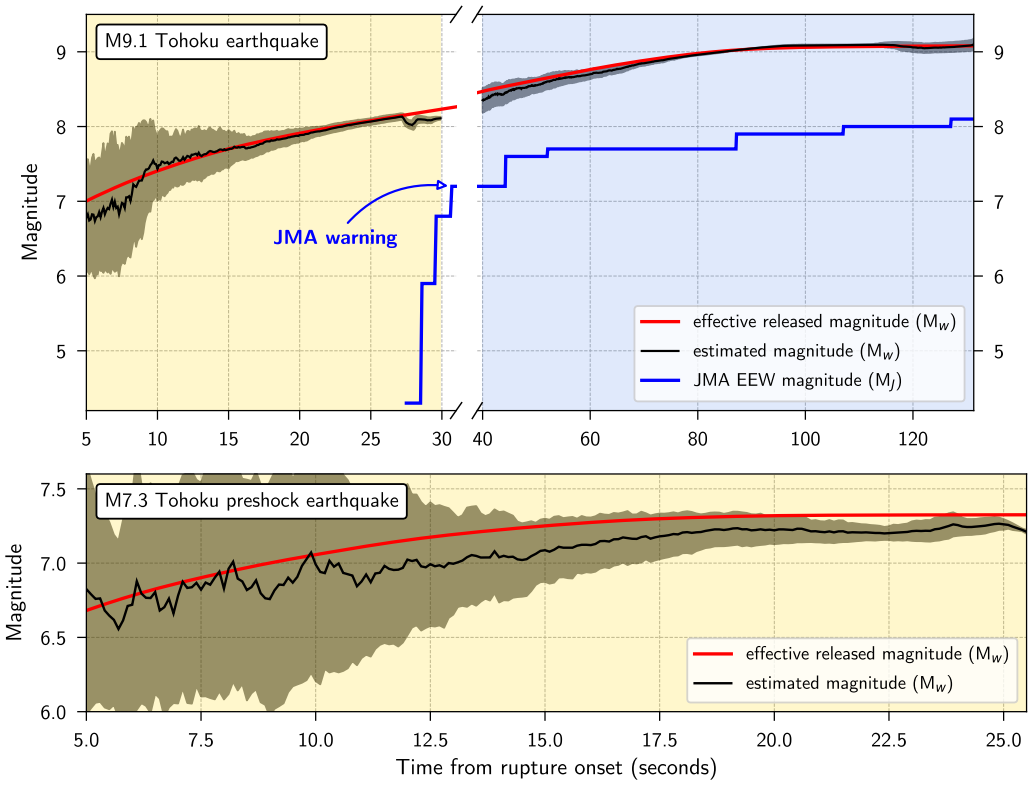

Figure 8. Rupture scenarii of the M9.1 Tohoku earthquake (top) and its M7.3 foreshock (bottom). The red lines represent the released magnitude (STF from the SCARDEC database), while the thick black lines represent the average estimated magnitudes over 100 iterations (bounded with the ± 1 standard deviation curves). The yellow panels indicate estimations provided by the network deployed close to the ruptured areas, and the blue panel estimations from the network at regional distance. Estimations are provided up to the seismic waves arrival at the network. The thick blue line represents the EEW magnitudes issued in real-time during the Tohoku earthquake by the JMA (Hoshiba & Ozaki, 2014).

To appreciate the magnitude uncertainties, we compute the standard deviation of the 100 estimated magnitudes from the random realizations. Based on the gravity strain data recorded by the local network, the LR exceeds 50 only 15 seconds after the Tohoku onset time, with a corresponding M7.70±0.26 magnitude estimate (the actual released moment is M7.7). For the foreshock, LR exceeds 50 only 18 seconds after the onset time, with a corresponding M7.21±0.14 magnitude estimate (actual released moment M7.31). In both cases, within 10 seconds of the rupture onset (at least 10 seconds before P-waves arrived to the coast) it could have been determined that the earthquake magnitude was likely to exceed M7. According to the SCARDEC STF, the Tohoku event released moment exceeded the M9 magnitude 83 seconds after its onset time. Our magnitude estimate based on gravity-strain data recorded by the regional network is, in this idealized exercise, in perfect agreement, as it reaches at that time M8.99±0.01.

Estimates of seismic moment M_0 based on early P- and S-wave signals are usually highly uncertain and underestimated (see for instance JMA warnings issued from seismic data in Fig. 8). Robust estimates of M_0 for large earthquakes based on W-phases (Kanamori & Rivera, 2008) can be obtained after at least 20 minutes (Duputel et al., 2011). Seismogeodetic methods based on high-rate GPS data can, in principle, provide rapid source parameter estimates within a few tens of seconds of the earthquake initiation (Crowell et al., 2016; Ruhl, Melgar, Grapenthin, & Allen, 2017). A robust estimate of M_0 derived from gravity signals might be obtained earlier, and fully stable at the end of the rupture, which could significantly enhance tsunami warning systems in the near-source region.

5 Conclusion

We have established key quantitative results regarding the capabilities that future gravity strainmeters could achieve for earthquake source characterization, based on earthquake-induced prompt gravity signals before direct seismic wave arrivals. We computed earthquake-induced prompt gravity strain signals with an analytical model in a homogeneous half-space, and tested various gravity strainmeters sensitivity models. Considering the planned sensitivities of about 10^{-15} $\mathrm{Hz}^{-1/2}$ at 0.1 Hz for the sub-Hz gravity strainmeters under development for GW detection, we have demonstrated that prompt perturbations induced by earthquakes larger than M7 can be observed with a single gravity detector at distances

shorter than 1000 km from the epicenter within the travel time of P-waves (SNR > 10), and up to 120 km within 10 seconds of the earthquake onset time (SNR > 5).

Since gravity field fluctuations propagate essentially instantaneously in comparison with seismic waves, a very promising application of this study is the improvement of the performance of EEWS. We demonstrate that a potential benefit of a gravity-based EEWS compared to seismic-based EEWS is earlier warning for large off-shore subduction earthquakes. Moreover, one of the current issues in EEWS is the estimation of the magnitude of the event, especially for mega earthquakes. Our simulations illustrate how gravity strainmeters could accelerate the estimation of the magnitude of mega earthquakes, by providing robust magnitude estimates within the duration of the fault rupture. We therefore propose that gravity strain data has the potential to complement other geophysical data in the future, to enhance tsunami warning systems.

While the foregoing discussion presents key elements of a gravity-based EEWS, a thorough assessment of the feasibility of this concept requires further developments: gravity signal predictions in more realistic earthquake scenarios that incorporate the effects of finite rupture size, Earth heterogeneities, attenuation and scattering, the analysis of the inverse problem of location and magnitude estimation to determine the optimal sensor network geometry, the assessment of the impact of non-stationary noise, and a cost-benefit analysis of its integration with existing EEWS. The most difficult challenge will be the development of gravity gradiometers with strain sensitivity of about 10^{-15} $\mathrm{Hz}^{-1/2}$ at 0.1 Hz.

Acknowledgments

We acknowledge the financial support from the UnivEarthS Labex program at Sorbonne Paris Cité (ANR-10-LABX-0023 and ANR-11-IDEX-0005-02) and the financial support of the Agence Nationale de la Recherche through the grant ANR-14-CE03-0014-01. JPM acknowledges the financial support of I.U.F. (Institut universitaire de France). We thank Tomofumi Shimoda for stimulating discussions. Numerical computations were partly performed on the S-CAPAD platform, IPGP, France.

References

Abbott, B., Abbott, R., Adhikari, R., Ajith, P., Allen, B., Allen, G., ... others

(2009). LIGO: the laser interferometer gravitational-wave observatory. *Reports on Progress in Physics*, *72*(7), 076901.

Accadia, T., Acernese, F., Antonucci, F., Astone, P., Ballardin, G., Barone, F., ... others (2011). Status of the Virgo project. *Classical and Quantum Gravity*, *28*(11), 114002.

Allen, R. (2013). Seismic hazards: Seconds count. *Nature*, *502*(7469), 29.

Allen, R. M., Gasparini, P., Kamigaichi, O., & Bose, M. (2009). The status of earthquake early warning around the world: An introductory overview. *Seismological Research Letters*, *80*(5), 682–693.

Ando, M., Ishidoshiro, K., Yamamoto, K., Yagi, K., Kokuyama, W., Tsubono, K., & Takamori, A. (2010). Torsion-bar antenna for low-frequency gravitational-wave observations. *Physical review letters*, *105*(16), 161101.

Beker, M., Cella, G., DeSalvo, R., Doets, M., Grote, H., Harms, J., ... others (2011). Improving the sensitivity of future GW observatories in the 1–10 Hz band: Newtonian and seismic noise. *General Relativity and Gravitation*, *43*(2), 623–656.

Böse, M., Allen, R., Brown, H., Gua, G., Fischer, M., Hauksson, E., ... others (2014). CISN ShakeAlert: An earthquake early warning demonstration system for California. In *Early warning for geological disasters* (pp. 49–69). Springer.

Böse, M., Heaton, T. H., & Hauksson, E. (2012). Real-time finite fault rupture detector (FinDer) for large earthquakes. *Geophysical Journal International*, *191*(2), 803–812.

Bose, S., Dayanga, T., Ghosh, S., & Talukder, D. (2011). A blind hierarchical coherent search for gravitational-wave signals from coalescing compact binaries in a network of interferometric detectors. *Classical and quantum gravity*, *28*(13), 134009.

Cella, G. (2000). Off-line subtraction of seismic Newtonian noise. In *Recent developments in general relativity* (pp. 495–503). Springer.

Cheinet, P., Canuel, B., Dos Santos, F. P., Gauguet, A., Yver-Leduc, F., & Landragin, A. (2008). Measurement of the sensitivity function in a time-domain atomic interferometer. *IEEE Transactions on instrumentation and measurement*, *57*(6), 1141–1148.

Colombelli, S., Zollo, A., Festa, G., & Picozzi, M. (2014). Evidence for a difference

in rupture initiation between small and large earthquakes. *Nature Communications*, *5*.

Crowell, B. W., Schmidt, D. A., Bodin, P., Vidale, J. E., Gomberg, J., Renate Hartog, J., ... others (2016). Demonstration of the Cascadia G-FAST geodetic earthquake early warning system for the Nisqually, Washington, earthquake. *Seismological Research Letters*, *87*(4), 930–943.

Driggers, J. C., Harms, J., & Adhikari, R. X. (2012). Subtraction of Newtonian noise using optimized sensor arrays. *Physical Review D*, *86*(10), 102001.

Duputel, Z., Rivera, L., Kanamori, H., Hayes, G. P., Hirshorn, B., & Weinstein, S. (2011). Real-time W phase inversion during the 2011 off the Pacific coast of Tohoku earthquake. *Earth, planets and space*, *63*(7), 5.

Dziewonski, A. M., & Anderson, D. L. (1981). Preliminary reference Earth model. *Physics of the earth and planetary interiors*, *25*(4), 297–356.

Ekström, G., Nettles, M., & Dziewoński, A. (2012). The global CMT project 2004–2010: Centroid-moment tensors for 13,017 earthquakes. *Physics of the Earth and Planetary Interiors*, *200*, 1–9.

Fiorucci, D., Harms, J., Barsuglia, M., Fiori, I., & Paoletti, F. (2018). Impact of infrasound atmospheric noise on gravity detectors used for astrophysical and geophysical applications. *arXiv preprint arXiv:1801.04564*.

Frank, W. B., Shapiro, N. M., Husker, A. L., Kostoglodov, V., Romanenko, A., & Campillo, M. (2014). Using systematically characterized low-frequency earthquakes as a fault probe in Guerrero, Mexico. *Journal of Geophysical Research: Solid Earth*, *119*(10), 7686–7700.

Geiger, R. (2017). Future gravitational wave detectors based on atom interferometry. In *An overview of gravitational waves: Theory, sources and detection* (pp. 285–313). World Scientific.

Gibbons, S. J., & Ringdal, F. (2006). The detection of low magnitude seismic events using array-based waveform correlation. *Geophysical Journal International*, *165*(1), 149–166.

Griggs, C., Moody, M., Norton, R., Paik, H., & Venkateswara, K. (2017). Sensitive superconducting gravity gradiometer constructed with levitated test masses. *Physical Review Applied*, *8*(6), 064024.

Harms, J. (2015). Terrestrial gravity fluctuations. *Living reviews in relativity*, *18*(1),

3.

Harms, J. (2016, feb). Transient gravity perturbations from a double-couple in a homogeneous half-space. *Geophysical Journal International*, *205*(2), 1153–1164. doi: 10.1093/gji/ggw076

Harms, J., Ampuero, J.-P., Barsuglia, M., Chassande-Mottin, E., Montagner, J.-P., Somala, S., & Whiting, B. (2015). Transient gravity perturbations induced by earthquake rupture. *Geophysical Journal International*, *201*(3), 1416–1425.

Harms, J., DeSalvo, R., Dorsher, S., & Mandic, V. (2009). Gravity-gradient subtraction in 3rd generation underground gravitational-wave detectors in homogeneous media. *arXiv preprint arXiv:0910.2774*.

Harms, J., & Paik, H. J. (2015). Newtonian-noise cancellation in full-tensor gravitational-wave detectors. *Physical Review D*, *92*(2), 022001.

Harms, J., Slagmolen, B. J., Adhikari, R. X., Miller, M. C., Evans, M., Chen, Y., ... Ando, M. (2013). Low-frequency terrestrial gravitational-wave detectors. *Physical Review D*, *88*(12), 122003.

Heaton, T. H. (1985). A model for a seismic computerized alert network. *Science*, *228*, 987–991.

Heaton, T. H. (2017). Correspondence: Response of a gravimeter to an instantaneous step in gravity. *Nature Communications*, *8*(1), 966.

Hogan, J. M., Johnson, D. M., Dickerson, S., Kovachy, T., Sugarbaker, A., Chiow, S.-w., ... others (2011). An atomic gravitational wave interferometric sensor in low earth orbit (AGIS-LEO). *General Relativity and Gravitation*, *43*(7), 1953–2009.

Hohensee, M., Lan, S.-Y., Houtz, R., Chan, C., Estey, B., Kim, G., ... Müller, H. (2011). Sources and technology for an atomic gravitational wave interferometric sensor. *General Relativity and Gravitation*, *43*(7), 1905–1930.

Hoshiba, M., & Ozaki, T. (2014). Earthquake early warning and tsunami warning of the Japan Meteorological Agency, and their performance in the 2011 off the pacific coast of Tohoku earthquake (Mw 9.0). In *Early warning for geological disasters* (pp. 1–28). Springer.

Houston, H. (2001). Influence of depth, focal mechanism, and tectonic setting on the shape and duration of earthquake source time functions. *Journal of Geophysical Research: Solid Earth*, *106*(B6), 11137–11150.

563 Jaranowski, P., & Królak, A. (2012). Gravitational-wave data analysis. formal-
564 ism and sample applications: the gaussian case. *Living Reviews in Relativity*,
565 *15*(1), 4.
566 Kanamori, H. (2005). Real-time seismology and earthquake damage mitigation.
567 *Annu. Rev. Earth Planet. Sci.*, *33*, 195–214.
568 Kanamori, H., & Rivera, L. (2008). Source inversion of W phase: speeding up seis-
569 mic tsunami warning. *Geophysical Journal International*, *175*(1), 222–238.
570 Madariaga, R. (1976). Dynamics of an expanding circular fault. *Bulletin of the Seis-*
571 *mological Society of America*, *66*(3), 639–666.
572 McManus, D., Forsyth, P., Yap, M., Ward, R., Shaddock, D., McClelland, D., &
573 Slagmolen, B. (2017). Mechanical characterisation of the TorPeDO: a low
574 frequency gravitational force sensor. *Classical and Quantum Gravity*, *34*(13).
575 Meier, M.-A., Ampuero, J., & Heaton, T. H. (2017). The hidden simplicity of sub-
576 duction megathrust earthquakes. *Science*, *357*(6357), 1277–1281.
577 Meier, M.-A., Heaton, T., & Clinton, J. (2016). Evidence for universal earthquake
578 rupture initiation behavior. *Geophysical Research Letters*, *43*(15), 7991–7996.
579 Meng, L., Allen, R., & Ampuero, J.-P. (2014). Application of seismic array process-
580 ing to earthquake early warning. *Bulletin of the Seismological Society of Amer-*
581 *ica*, *104*(5), 2553–2561.
582 Minson, S. E., Murray, J. R., Langbein, J. O., & Gomberg, J. S. (2014). Real-time
583 inversions for finite fault slip models and rupture geometry based on high-rate
584 GPS data. *Journal of Geophysical Research: Solid Earth*, *119*(4), 3201–3231.
585 Montagner, J.-P., Juhel, K., Barsuglia, M., Ampuero, J. P., Chassande-Mottin, E.,
586 Harms, J., ... Lognonné, P. (2016, nov). Prompt gravity signal induced by
587 the 2011 Tohoku-oki earthquake. *Nature Communications*, *7*, 13349. doi:
588 10.1038/ncomms13349
589 Moody, M. V., Paik, H. J., & Canavan, E. R. (2002). Three-axis superconducting
590 gravity gradiometer for sensitive gravity experiments. *Review of scientific in-*
591 *struments*, *73*(11), 3957–3974.
592 Nakamura, Y., & Saita, J. (2007). UrEDAS, the earthquake warning system: Today
593 and tomorrow. In *Earthquake early warning systems* (pp. 249–281). Springer.
594 Pai, A., Dhurandhar, S., & Bose, S. (2001). Data-analysis strategy for detecting
595 gravitational-wave signals from inspiraling compact binaries with a network of

laser-interferometric detectors. *Physical Review D*, *64*(4), 042004.

Paik, H. J., Griggs, C. E., Moody, M. V., Venkateswara, K., Lee, H. M., Nielsen, A. B., ... Harms, J. (2016). Low-frequency terrestrial tensor gravitational-wave detector. *Classical and Quantum Gravity*, *33*(7), 075003.

Porter, K. A. (2016). How many injuries can be avoided through earthquake early warning and drop, cover, and hold on? [Computer software manual]. Retrieved from `https://www.colorado.edu/ceae/sites/default/files/attached-files/porter-2016-cu-eew-dcho.pdf`

Ruhl, C., Melgar, D., Grapenthin, R., & Allen, R. (2017). The value of real-time GNSS to earthquake early warning. *Geophysical Research Letters*, *44*(16), 8311–8319.

Shelly, D. R., Beroza, G. C., & Ide, S. (2007). Non-volcanic tremor and low-frequency earthquake swarms. *Nature*, *446*(7133), 305.

Shimoda, T., Aritomi, N., Shoda, A., Michimura, Y., & Ando, M. (2018). Seismic cross-coupling noise in torsion pendulums. *Physical Review D*, *97*(10), 104003.

Shoda, A., Ando, M., Ishidoshiro, K., Okada, K., Kokuyama, W., Aso, Y., & Tsubono, K. (2014). Search for a stochastic gravitational-wave background using a pair of torsion-bar antennas. *Physical Review D*, *89*(2), 027101.

Takamatsu, K. (2009). Application of the earthquake early warning system for the OKI semiconductor factory. In *The 2nd international workshop on earthquake early warning.*

Vallée, M., Ampuero, J. P., Juhel, K., Bernard, P., Montagner, J.-P., & Barsuglia, M. (2017). Observations and modeling of the elastogravity signals preceding direct seismic waves. *Science*, *358*(6367), 1164–1168.

Vallée, M., Charléty, J., Ferreira, A. M., Delouis, B., & Vergoz, J. (2011). SCARDEC: a new technique for the rapid determination of seismic moment magnitude, focal mechanism and source time functions for large earthquakes using body-wave deconvolution. *Geophysical Journal International*, *184*(1), 338–358.

Winterflood, J. (2001). *High performance vibration isolation for gravitational wave detection* (Unpublished doctoral dissertation). University of Western Australia Perth.

Zollo, A., Amoroso, O., Lancieri, M., Wu, Y.-M., & Kanamori, H. (2010). A

threshold-based earthquake early warning using dense accelerometer networks. *Geophysical Journal International*, *183*(2), 963–974.